are combined into a detector array of up to 6 224 001 pixels. A further development of the PILATUS detector is the EIGER detector (Johnson *et al.*, 2014). The system consists of single-photon-counting modules of 256 × 256 pixels with a significantly reduced pitch of only 75 × 75 μm. Like GOTTHARD, the charge-integrating equivalent of MYTHEN, the JUNGFRAU detector (Mozzanica *et al.*, 2014) was developed as a charge-integrating equivalent to the PILATUS and EIGER detectors.

Even smaller pixel sizes of 55 × 55 μm have been achieved for the hybrid pixel detector Medipix3 (Ballabriga *et al.*, 2007). Modules of 256 × 256 pixels can be combined into large arrays. The electronics are highly configurable and allow charge summing, programmable binary counter and continuous count–read modes.

In principle, fast data collection seems to be desirable, but it has to be adjusted to the process that is being investigated. In most cases for a continuous frame rate the limiting factor is the data rate. The MYTHEN II detector (Schmitt *et al.*, 2003) installed at the Swiss Light Source allows a frame rate of 10–90 Hz, depending on the desired dynamic range (24–4 bits), and thus observations in the time range below 1 s to 10 ms. The two-dimensional detectors for high-energy X-rays can operate at a maximum of 30 Hz (Perkin Elmer) or 60 Hz (Pixium). In this context it is also worth mentioning the PILATUS detectors – a series of silicon pixel detectors also developed at the Swiss Light Source and further commercialized by Dectris. These detectors possess a high dynamic range over five orders of magnitude along with a rate capability of $>2 \times 10^6$ photons s^{-1} $pixel^{-1}$ and excellent detection efficiency of nearly single-photon counting (99% at 8 keV and 55% at 15 keV). The use of 1000 μm-thick CdTe instead of silicon enables >90% quantum efficiency at 20 keV, 81% at 40 keV, 90% at 60 keV, 77% at 80 keV and 56% at 100 keV. Complex detectors are often characterized by a long readout time of a large number of two-dimensional pixels, *e.g.* for PILATUS detectors the readout time per module is ∼2.7 ms.

Semiconductor-based detectors can operate at significantly higher frame rates. The EIGER detector can operate at a maximum frame rate of 24 kHz, while GOTTHARD can reach 40 kHz. In a special burst mode of 128 frames, a frame rate of 800 kHz is possible, reaching a single exposure time of 1.25 μs. The Timepix3 detector (Poikela *et al.*, 2014), which is a further development of the Medipix3 detector, can theoretically sustain continuous frame rates of up to 200 kHz, as long as the overall hit rate is less than 80 MHz.

In order to collect enough intensity for fast processes or to investigate even shorter timescales, stroboscopic measurements are useful. Thus, timescales in the range of milliseconds down to nanoseconds may be followed using a pump–probe setup. In this technique, the reaction is first triggered (pump) and after a specific time delay the diffraction pattern is collected (probed). The use of rapidly rotating choppers in the incoming beam is an attractive alternative to pump–probe experiments (Yoo *et al.*, 2011). Time resolution in the microsecond regime is routinely obtained in synchrotron experiments (Hinterstein, 2011; Hinterstein *et al.*, 2014) and in about the millisecond regime in neutron diffraction (Eckold *et al.*, 2010). When these experiments are conducted at a synchrotron and the periodic excitation of the sample is synchronized with the bunch clock of the synchrotron, the time resolution can be increased significantly. For a time resolution smaller than the temporal separation of the particle bunches (typically 8–200 ns), the time resolution suddenly drops to the bunch width, which is in the range of picoseconds. For neutron diffraction, the limiting factor for time resolution can be calculated from the energy bandwidth and the speed of the neutrons, which is dependent on the wavelength. The lower limit is typically in the range of 25 μs. These time ranges can be reached by multistrip or multiwire detectors in a stroboscopic setup.

In situ and *in operando* measurements require a specific sample environment, which is normally built using a different material to the sample and leads to additional contributions to the diffraction pattern. The use of strongly scattering materials such as thin metallic foils (Al foil in batteries, Ag or Au films as electrodes) or single crystals (sapphire capillaries for high-temperature experiments or diamonds in high-pressure experiments) may seriously bias data collection or damage the detector. If it is not possible to eliminate them by masking, they have to be taken into account by Rietveld analysis or profile matching. A correct treatment of the contributions from the sample environment has to take into consideration the fact that the additional scattering is normally off the diffractometer centre and this sample shift produces a non-linear shift in 2θ of the corresponding reflections in the pattern.

2.8.2.2. *Absorption*

Additional equipment is required for *in situ* experiments. The necessary parts are quite often constructed from metallic components. Light metals like aluminium are preferred for shielding parts within the beam for neutrons and X-rays. Vanadium is a suitable choice in neutron experiments, as it has a very small scattering cross section, so produces almost no coherent scattering. In most cases a suitable absorption correction is mandatory. For X-rays the energy dependence of the linear absorption coefficient $\mu(E)$ is very pronounced, especially close to X-ray absorption edges. Away from an absorption edge, higher energies lead to lower absorption. As an example, the linear absorption coefficient μ for steel (α-Fe) at 45 keV is 0.18 cm^{-1} and at 60 keV it is 0.076 cm^{-1}. The transmitted intensity after a beam has penetrated 1 mm steel with 100% packing density twice (once for the incoming and once for the outgoing beam) is therefore 2.7% for 45 keV but 22% for 60 keV. For one of the examples treated later, the piezoceramic $Pb(Zr_{0.5}Ti_{0.5})O_3$, the calculation for a sample diameter of 1 mm and a typical packing density of 60% in a powder leads to beam transmission of 3% (45 keV) and 21% (60 keV). Therefore, using high-energy X-rays enables transmission diffraction experiments that are not feasible with lower energies. The gain in measured intensities by decreasing absorption normally overcompensates for the decrease in scattering at shorter wavelengths, which is proportional to λ^3 within kinematical theory. The linear absorption coefficient of thermal neutrons (with wavelengths from 1 to about 3 Å) is small for most elements and scales in proportion to the wavelength, $\lambda = h/p = h/(2mE)^{1/2}$, *i.e.* λ (Å) = $9.045/E^{1/2}$ (meV) = $3956/v$ (m s^{-1}). However, the absorption cross sections for different isotopes of the same element may be very different. Numerical values are listed in Sears (1992) and *International Tables for Crystallography* Volume C, Table 4.4.4.1. For ferroelectric $Pb(Zr_{0.5}Ti_{0.5})O_3$, the linear neutron absorption coefficient at a wavelength λ = 1.5 Å and for a packing density of 60% is 0.026 cm^{-1}, significantly smaller than for X-rays; it is mainly determined by the Ti content.

As both the scattering and the absorption cross section for neutrons are in most cases much smaller than for X-rays, bigger samples are required. On the one hand, this leads to the advantage of better averaging over many particles. On the other hand,

the spatial resolution is significantly affected by the sample dimensions because of self-collimation. The appropriate choice of diffraction method is defined by the particular scientific challenge and has to take into consideration the different amount of sample that is needed for each experiment.

Very high absorption cross sections are desirable for shielding purposes. In X-ray diffraction, lead or tungsten are widely used. Only a few isotopes have a nuclear resonance in the thermal neutron range and thus a high absorption cross section. The most prominent are ^{10}B, ^{113}Cd and ^{157}Gd, which are used in neutron optics as collimators, attenuators and beam-shaping devices.

2.8.2.3. *Sample fluorescence and incoherent neutron scattering*

Sample fluorescence is a common problem for laboratory X-ray powder diffractometers, which are neither equipped with an analyser nor use detectors with a narrow energy resolution. In powder diffraction using synchrotron radiation, this problem is often solved either by adjusting the energy of the incident beam or by an adjustment of the dynamic range of the detector, or by a combination of both.

Like absorption cross sections, the incoherent neutron scattering lengths for different elements and isotopes do not vary in any obviously systematic way throughout the periodic table. Among the known stable isotopes, ^{1}H has the largest incoherent scattering length (25.274 fm) and has a small and negative coherent one (−3.7406 fm). The situation is very different for ^{2}H (deuterium), for which the incoherent and coherent scattering lengths are 4.04 and 6.671 fm, respectively. Differences between the coherent scattering lengths of hydrogen and deuterium form the basis of the isotopic labelling technique, called contrast matching; this is particularly important in applications of neutron scattering to hydrogen storage, structural biology and polymer science. Deuteration of samples is a challenging task, but obtaining high-quality powder diffraction data from hydrogenated samples is far more difficult. Use of neutron polarization analysis is a reliable way to subtract the incoherent scattering contribution from the diffraction data (Mikhailova *et al.*, 2012), but it is often accompanied by significant losses of incident neutron flux and, consequently, of data quality. Both sample fluorescence and incoherent neutron scattering are isotropic and, therefore, are often considered as a background in powder diffraction experiments.

2.8.3. Examples

2.8.3.1. *In situ studies of ferroelectrics in an external electric field*

The function of ferroelectrics as stress sensors, high-frequency microphones, medical injectors or large strain actuators is based on electric poling. A polycrystalline material exhibits a zero net polarization. When an electric field is applied to the sample, the spontaneous electric polarization of the ferroelectric material is reoriented along the electric field vector. This occurs by a reorientation of domains. Additional polarization is obtained by an increase of the spontaneous polarization induced by the applied electric field. With *in situ* experiments, the field-induced changes in the powder diffraction reflections are measured. Fig. 2.8.1 is a schematic representation of some *in situ* sample geometries. The electric field is applied *via* electrodes on the sample surface.

Many of these ferroelectric materials crystallize in a structure derived from the cubic perovskite type, but in a crystal system with lower symmetry and with a non-centrosymmetric space group. The most widely used material is lead zirconate-titanate ($PbZr_{1-x}Ti_xO_3$, PZT), which exhibits the highest strain response

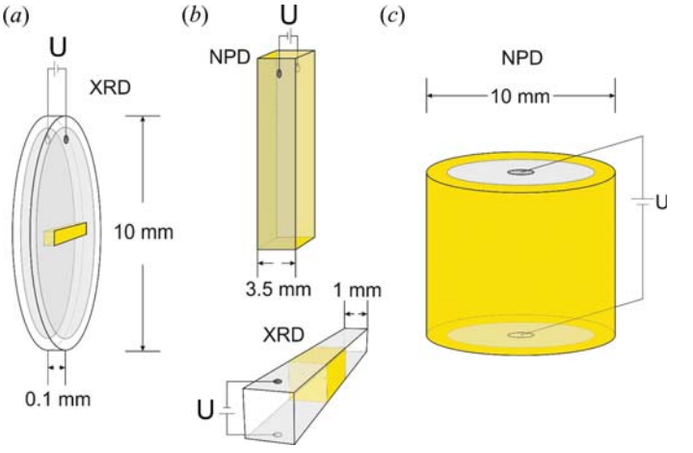

Figure 2.8.1
Sample geometries for *in situ* experiments with an applied electric field. Samples are poled *via* an applied voltage (U) at the sample electrodes (grey). Different sample geometries are necessary to account for different beam sizes, absorption and detector concepts. Yellow indicates the irradiated sample volume. (*a*) Flat-plate samples for X-ray experiments with strip detectors, limiting photon energies to around 30 keV. (*b*) Bar-shaped samples for high-intensity neutron powder diffraction (NPD) or high-energy X-ray diffraction (XRD). (*c*) Cylinder-shaped samples for high-resolution neutron diffraction with fixed detector collimators.

at the so-called morphotropic phase boundary with a composition of about 50% for Ti and Zr. It is generally accepted that the phase on the Ti-rich side of the PZT phase diagram has a tetragonal structure with space group *P*4*mm*. On the rhombohedral Zr-rich side, two ferroelectric phases can be identified, with space groups *R*3*m* for high and *R*3*c* for low temperatures. A considerable amount of work has been devoted to the elucidation of the crystal structure of the material close to the morphotropic phase boundary. Neutron and synchrotron diffraction detected monoclinic symmetry at low temperatures and nanometre-sized regions (the so-called polar nanoregions) were inferred from diffuse scattering (Noheda *et al.*, 2000; Hirota *et al.*, 2006). Alternative interpretations explained the new reflection found in the pattern between the 111_C and 200_C reflections (where the subscript 'C' corresponds to the cubic archetype structure) as diffuse scattering from diffuse incoherent scattering by small domains (Jin *et al.*, 2003).

Unique information on structural changes during poling is obtained from *in situ* studies in applied external electric fields (Hoffmann *et al.*, 2001). Fig. 2.8.2 displays two groups of powder reflections (Schönau, Schmitt *et al.*, 2007) observed by synchrotron X-ray diffraction. They are directly compared with the domain structure from TEM observations (Schmitt *et al.*, 2007) for a range of compositions near the morphotropic phase boundary. One group of reflections is derived from the cubic 111_C reflection, the other from the archetype 200_C reflection. The transition from the rhombohedral splitting to the tetragonal one with increasing Zr content is correlated with the forms of ferroelectric domains in TEM. Close to the morphotropic phase boundary, nanodomains (ranging in width from 20 to 200 nm) are observed in addition to the well known microdomains. The nanodomains react immediately under the influence of an electric field to become microdomains. Fig. 2.8.3 shows the intensity changes observed for the 110_C group of reflections. The changes under an electric field are pronounced and depend on the *c*/*a* ratio (Schönau, Knapp *et al.*, 2007), the formation and disappearance of nanodomains, and the local symmetry of these domains.

references